

Dark Matter Induced Power in Quantum Devices

Anirban Das,^{1,*} Noah Kurinsky,^{1,2,†} and Rebecca K. Leane^{1,2,‡}

¹SLAC National Accelerator Laboratory, 2575 Sand Hill Rd, Menlo Park, CA 94025, USA

²Kavli Institute for Particle Astrophysics and Cosmology, Stanford University, Stanford, CA 94035, USA

(Dated: October 17, 2022)

We present single quasiparticle devices as new dark matter (DM) detectors. The threshold of these devices is set by the cooper pair binding energy, and is therefore so low that they can detect DM as light as about an MeV incoming from the Galactic halo, as well as the low-velocity thermalized DM component potentially present in the Earth. Using existing power measurements with these new devices, as well as power measurements with SuperCDMS-CPD, we set new constraints on the DM scattering cross section for DM masses from about 1 MeV to 10 GeV, down to about $10^{-34} - 10^{-26}$ cm² for spin-independent interactions. We outline future directions to improve sensitivity to both halo DM and a thermalized DM population in the Earth using power deposition in quantum devices.

Introduction.— At any given moment, a powerful stream of DM particles from the Galactic halo flows into the Earth. This Galactic DM has been extensively searched for in direct detection experiments, which aim to detect recoil events when DM scatters off the Standard Model (SM) target material, thereby providing a test of the DM-SM scattering cross section. Typically, the energy threshold of direct detection experiments assuming nuclear recoils is about a keV, corresponding to the recoil expected for DM with mass above about a GeV for standard analyses [1], or MeV-scale masses when exploiting the Migdal effect [2–6] or electron recoils [7–9].

Given the lack of a conclusive DM detection with direct detection experiments so far, interest in novel detection strategies and new devices has exploded in the last few years [10]. In particular, the race down to increasingly low thresholds has inspired use of new detectors, including superconductors [11–16], superfluids [17–19], polar crystals [20–22], topological materials [23], and Dirac materials [24–27]. Superconductors show exceptional promise, due to their superconducting energy gaps as low as about an meV, allowing probes of light DM.

The goal of lower threshold experiments to date has been to push down sensitivity to lower DM masses, and we will exploit this to test incoming halo DM down to about an MeV. We also point out that lowered thresholds open up a new probe of a DM component other than the usually-considered halo DM: the DM population that is already thermalized and bound. When the Galactic halo DM enters the Earth, it scatters, loses energy, and can become gravitationally captured. Over time, this builds up a thermalized population of DM particles bound to the Earth. For DM around a few GeV that is in local thermal equilibrium, the density of bound DM at Earth’s surface can in fact be enormous: about 15 orders of magnitude higher than the local DM halo density. Unfortunately this large density enhancement is lost on traditional direct detection experiments, as the bound DM population

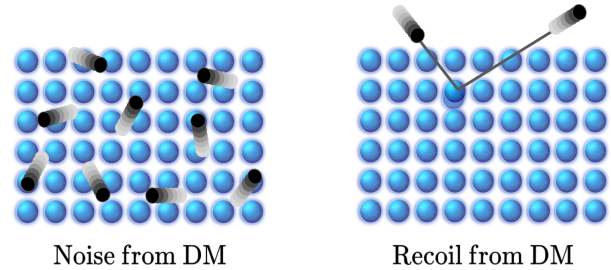


Figure 1. The qualitative difference between our proposal and a conventional DM direct detection experiment. The noise arises from *frequent* interaction between DM and the nuclei in the detector, as opposed to *once-in-a-while recoil* of a nucleus from DM scattering.

has a very low velocity compared to halo DM, requiring thresholds of less than about 0.05 eV at Earth’s surface.

We will demonstrate for the first time that new quantum devices can be used to detect DM with low energy depositions. This includes sensitivity to both light DM from the halo, as well as thermalized bound DM. As schematically shown in Fig. 1, for thermalized DM our proposal exploits their high DM density and is sufficiently sensitive despite low thermal velocities, compared to traditional direct detection, which only measures the less frequent and higher-velocity DM halo interactions. We point out and will use the fact that both halo DM and thermalized DM would produce excess quasiparticle generation in single quasiparticle devices, and excess power produced in athermal phonon sensors, to set new constraints on DM with interaction cross sections larger than about $10^{-34} - 10^{-28}$ cm² for DM masses of ~ 300 MeV–10 GeV for thermalized DM. For halo DM, we will set new constraints down to about $10^{-29} - 10^{-26}$ cm² for DM masses of ~ 1 MeV–10 GeV.

We now detail the DM distribution at Earth’s surface, before discussing the scattering rate and energy deposition in quantum devices. We then will show both the halo DM and thermalized DM signal detectability and new constraints, and conclude with the outlook for discovering DM with quantum devices going forward.

* Email: anirband@slac.stanford.edu

† Email: kurinsky@slac.stanford.edu

‡ Email: rleane@slac.stanford.edu

Dark Matter at Earth’s Surface.— At Earth’s position, there are two potential DM components present, which have different DM velocity and density assumptions. We will test both of these components. One is DM incoming from the Galactic halo, which is usually assumed for direct detection experiments. The other is the thermalized DM component. This thermalized component exists as once DM enters the Earth, it can thermalize, and become captured and bound to the Earth. For sufficiently large DM-SM scattering cross sections (larger than about 10^{-35} cm²), the DM rapidly thermalizes and is said to be in local thermal equilibrium with the surrounding SM matter. In this case, the DM radial profile within the Earth, n_χ , is dominantly governed by the differential equation [28]

$$\frac{\nabla n_\chi}{n_\chi} + (\kappa + 1) \frac{\nabla T}{T} + \frac{m_\chi g}{T} = \frac{\Phi}{n_\chi D_{\chi N}} \frac{R_\oplus^2}{r^2}, \quad (1)$$

where T is the Earth’s radial temperature profile at position r , R_\oplus is Earth’s radius, m_χ is the DM mass, g is gravitational acceleration, and Φ is the incoming flux of DM particles from the Galactic halo. $D_{\chi N} \sim \lambda v_{\text{th}}$ and $\kappa \sim -1/[2(1 + m_\chi/m_{\text{SM}})^{3/2}]$ are diffusion coefficients, with λ the DM mean free path, v_{th} the DM thermal velocity, and m_{SM} the SM target mass. The DM density profile is normalized by enforcing that its volume integral equals the total number of particles expected within in the Earth; see Ref. [28] for details, which provides the full DM distribution calculation for arbitrary celestial objects. Note that Eq. (1) assumes rapid thermalization, which will be valid for our parameter space of interest.

Solving Eq. (1) for $n_\chi(r)$ reveals that this thermalized population of DM can be significantly more abundant at the Earth’s surface than the incoming halo DM particles. For DM masses around a GeV, the local DM density can be as high as about $\sim 10^{14}$ cm⁻³. However, as this population is thermalized within the Earth, its velocity is low. We approximate the thermalized DM velocity distribution as a truncated Maxwell-Boltzmann distribution,

$$f_\chi(\mathbf{v}) = \frac{1}{N_0} e^{-(\mathbf{v}/v_{\text{th}})^2} \Theta(v_{\text{esc}} - v), \quad (2)$$

where N_0 normalizes the distribution, and $v_{\text{th}}^2 = 8T_\chi/\pi m_\chi$ with $T_\chi \simeq 300$ K. This velocity would require thresholds of $E \lesssim 0.05$ eV for conventional detection techniques. This is much lower than the reach of typical direct detection experiments, and so requires new techniques to be detected.

For halo DM, in Eq. (2) v_{th} is replaced by the average DM velocity in the halo $v_0 = 230$ km/s. In this case, the relative velocity between the Earth and DM also becomes important. Hence, for halo DM we use the boosted velocity $\mathbf{v} \rightarrow \mathbf{v} + \mathbf{v}_\oplus$ in Eq. (2), where $|\mathbf{v}_\oplus| = 240$ km/s is the Earth’s velocity in the galactic rest frame. The halo DM density is assumed to be 0.4 GeV cm⁻³. We will now show for the first time that new quantum devices are highly sensitive to

DM with low energy depositions, which includes both the thermalized DM population, as well as light halo DM.

Scattering Rate & Energy Deposition.— As a DM particle with velocity \mathbf{v} scatters in the detector and transfers momentum \mathbf{q} , it deposits an amount of energy

$$\omega_{\mathbf{q}} = \mathbf{q} \cdot \mathbf{v} - \frac{q^2}{2m_\chi} = E_f - E_i. \quad (3)$$

As a result, the target makes a transition from $|i\rangle$ to $|f\rangle$. For such low energy depositions, the momentum transferred is comparable to the inverse size of nuclear wavefunction in a detector crystal, and the inter-atomic forces become important. Hence, lattice vibrations or phonon excitations will be used to compute the DM scattering rate. The total rate per target mass can be written as [29, 30]

$$\Gamma = \frac{\pi \sigma_{\chi N} n_\chi}{\rho_T \mu^2} \int d^3 v f_\chi(\mathbf{v}) \int \frac{d^3 q}{(2\pi)^3} F_{\text{med}}^2(\mathbf{q}) S(\mathbf{q}, \omega_{\mathbf{q}}) \quad (4)$$

Here, $f_\chi(\mathbf{v})$ is DM velocity distribution, ρ_T is the target density, $\sigma_{\chi N}$ is the DM-nucleon scattering cross section, μ is the reduced mass of the DM-nucleon system, $F_{\text{med}}(\mathbf{q})$ is a form-factor that depends on the mediator (we will assume $F_{\text{med}}(\mathbf{q}) = 1$), and $S(\mathbf{q}, \omega_{\mathbf{q}})$ is the dynamic structure factor containing the detector response to DM scattering and depends on the crystal structure of the target material. The differential rate as a function of deposited energy ω can be written by inserting a delta function

$$\frac{d\Gamma}{d\omega} = \frac{\pi \sigma_{\chi N} n_\chi}{\rho_T \mu^2} \int d^3 v f_\chi(\mathbf{v}) \times \int \frac{d^3 q}{(2\pi)^3} F_{\text{med}}^2(\mathbf{q}) S(\mathbf{q}, \omega) \delta(\omega - \omega_{\mathbf{q}}). \quad (5)$$

To compute DM scattering rates, we follow Refs. [31, 32] and use the publicly available code DarkELF. We modify DarkELF in two main ways. Firstly, we update the local DM density and DM velocity input to be that described in the previous section, for halo or thermalized DM as appropriate. Secondly, the code was developed only for materials with two atoms per primitive cell, which is smallest unit cell. Thus, we adapt it for materials like Al which has only one atom in its primitive cell.

As described in Refs. [32–34], in the incoherent scattering regime the structure factor is approximated by

$$S(\mathbf{q}, \omega) \approx \frac{2\pi}{V_c} f^2 e^{-2W_d(\mathbf{q})} \sum_n \left(\frac{q^2}{2m_A} \right)^n \times \frac{1}{n!} \left(\prod_{i=1}^n \int d\omega_i \frac{D_d(\omega_i)}{\omega_i} \right) \delta \left(\omega - \sum_i \omega_i \right). \quad (6)$$

Here V_c is the primitive cell volume, m_A is the mass of a target atom, n is the number of phonons excited, $W_d(\mathbf{q})$ is the Debye-Waller function (see Eq. (S8)), and $D_d(\omega)$ is the phonon density of states (DoS). The

average phonon energy $\bar{\omega}_d$, determined by the DoS of the material, determines the typical number of phonons, $n \sim q^2/(2m_A\bar{\omega}_d)$. In Eq. (6), we take $f = A$ as the coupling for spin-independent interactions, where the scattering benefits from nuclear coherence.

Detection Mechanisms and Materials.— Detecting light halo DM or the captured DM population of low thermal energy demands use of low threshold quantum sensors that can detect $\sim \mathcal{O}(10)$ meV energy deposition. Such sensors are usually designed using superconducting materials, which have vitally small energy gaps [35–38]. Aluminum (Al) is a widely used superconductor for such a purpose and its characterization data is readily available. Such small amount of energy transfer is not sufficient for nuclear recoil or electronic ionization, however DM can excite collective modes, such as phonons in the material, resulting in an excess power. For example, in one experimental setup, a bias circuit stabilizes the absorber material at its transition temperature T_c , where its resistance is very sensitive to any energy deposition. The total power deposited in the detector by DM in the form of phonons can be obtained from Eq. (5) for the target material as

$$P_{\text{DM}} = \epsilon \int d\omega \omega \frac{d\Gamma}{d\omega}, \quad (7)$$

where ϵ is an efficiency factor that depends on the experimental setup. We will use this to calculate excess power due to DM and set constraints on DM-SM interactions. Volume-scaled detectors based on conventional semiconductors, such as Si, can also be used as the absorber material to look for ambient power deposition; the power deposited per unit volume can be obtained from Eq. (7).

We also consider excess quasiparticle production from DM. In a superconducting metal, the electrons are bound into Cooper pairs through a long-range interaction with phonons. When a DM particle scatters with a nucleus, it may deposit its kinetic energy in the form of phonons. If the deposited energy exceeds the energy gap Δ of the superconductor, these excess phonons will break some of the Cooper pairs and release quasiparticles above the gap. We will therefore set limits on DM-SM interactions by calculating quasiparticle production rates from DM.

The quasiparticle generation rate R_{qp} by DM scattering can be written as

$$R_{\text{qp}} = \frac{\epsilon_{\text{qp}}}{\Delta} \int d\omega \omega \frac{d\Gamma}{d\omega} \approx \left(\frac{P_{\text{DM}}}{9 \times 10^{-23} \text{ W}\mu\text{m}^{-3}} \right) \frac{\text{qps}}{\text{s} \cdot \mu\text{m}^3}, \quad (8)$$

where P_{DM} is the deposited DM power above the gap in $\text{W}\mu\text{m}^{-3}$, assuming a 60% quasiparticle generation efficiency ($\epsilon_{\text{qp}} = 0.6$) [14, 39], and using $\Delta \simeq 340 \mu\text{eV}$ for Al.

A conservative estimate of c , the steady-state quasiparticle density, can be found using mean field results

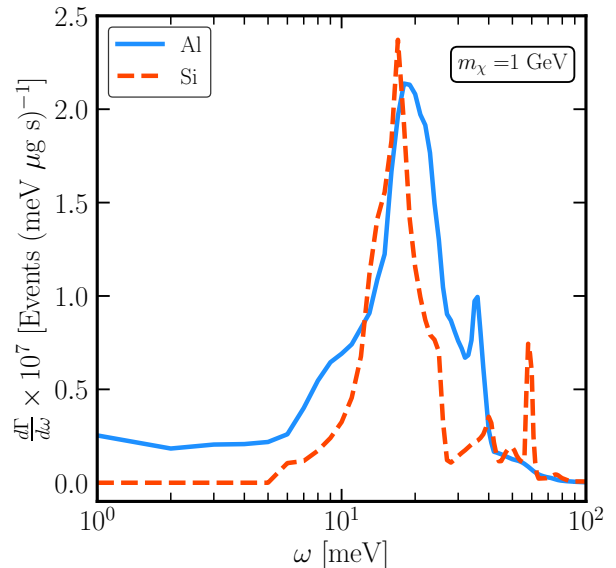


Figure 2. Differential scattering rate for thermalized DM in Al and Si for $m_\chi = 1 \text{ GeV}$ and $\sigma_{\chi N} = 10^{-30} \text{ cm}^2$.

from Ref. [40]. There, $c = \sqrt{R_{\text{qp}}/\bar{\Gamma}}$, with $\bar{\Gamma} = 40 \text{ s}^{-1}\mu\text{m}^3$ for Al. The steady-state density is therefore

$$c \approx \left(\frac{P_{\text{DM}}}{3.6 \times 10^{-21} \text{ W}} \right)^{1/2}, \quad (9)$$

which can be compared to known measurements to set new constraints.

Figure 2 shows example event rates for thermalized DM in both Al and Si, scattering cross sections of $\sigma_{\chi N} = 10^{-30} \text{ cm}^2$. We obtain our event rates by using Eq. (5), with the dynamic structure factor from Eq. (6).

Detecting Dark Matter with Single Quasiparticle Devices.—

(i) *Quasiparticle Background Devices:* Quasiparticle excitations formed from broken Cooper pairs are important to minimize in quantum devices, as the quasiparticle background limits the operation of applications such as radiation detectors and superconducting quantum computers. To test how low of a quasiparticle background might be possible, Ref. [35] constructed a mesoscopic superconducting island, and studied the number of quasiparticles by monitoring single-electron tunneling. Ref. [35] found the device remained free from quasiparticles for up to seconds, producing the lowest limit on quasiparticle density of $0.013 \text{ qps}\mu\text{m}^{-3}$ [35]. We convert this measurement to a power density, finding an upper limit of $6 \times 10^{-25} \text{ W}\mu\text{m}^{-3}$. Given that this measurement is a power that continues to decay exponentially with time cold, we can consider this an upper limit on residual power injection. We therefore point out that quasiparticles produced by DM, and therefore the DM-SM scattering rate, can be constrained using devices with low-quasiparticle density backgrounds. Interestingly, it

is not known what currently produces the quasiparticles measured in these devices [35, 41–44]. We point out for the first time that it could correspond to detection of DM, but caution that this requires proper studies of systematics which at this point are lacking.

(ii) *Low Noise Bolometers:* Understanding our Universe deep into the infrared would reveal new secrets of galaxy formation, exoplanets, and so much more. However, far-infrared spectroscopy requires new cryogenic space telescopes with technologies capable of measuring very cold objects, and therefore require low noise equivalent power in their detectors. Adapting technology from quantum computing applications, Ref. [36] developed a quantum capacitance detector where photon-produced free electrons in a superconductor tunnel into a small capacitive island. This setup is embedded in a resonant circuit, and therefore can be referred to as a “quantum resonator”. This quantum resonator measured excess power of 4×10^{-20} W [36], making it the most sensitive existing far-infrared detector. The volume of absorber used in this case was a mesh grid, roughly 60 microns square with a 1% fill factor and 60 nm thick. This corresponds to a volume of around $2.3 \mu\text{m}^3$ and thus a power density measurement of $1.7 \times 10^{-20} \text{ W}\mu\text{m}^{-3}$. We therefore point out that single quasiparticle devices can be used for DM detection through their power measurements, and will use this current measurement to set constraints on the DM-SM scattering rate which would produce excess power. Note that this detector has a calibrated external efficiency of greater than 95%, which reduces the systematic uncertainty on the power limit. Ref. [36] excludes the possibility that this is induced by residual radiation and represents a true, measured excess power.

Detecting DM Power Deposition with Existing DM Detectors.— While we have pointed out new devices that can be used as DM detectors above, we also point out for the first time that more conventional quantum sensors with volume-scaling can already be used to constrain low-energy deposition DM. We consider SuperCDMS detectors, which have recorded volume-scaled transition-edge sensor (TES) bias power measurements in which the TES is coupled to a large aluminum absorber [38]. For Refs. [38] we find a bias power of 2×10^{-15} fW, and an Al absorber with a volume of $2 \times 10^6 \mu\text{m}^3$. This yields a power density of order $10^{-21} \text{ W}\mu\text{m}^{-3}$. The coupling efficiency of power to the readout in this case is 30% ($\epsilon = 0.3$), so our bound on DM power using Al would be $3 \times 10^{-21} \text{ W}\mu\text{m}^{-3}$. However, the best constraints on DM scattering power injection come from SuperCDMS-CPD [37], which instead has 10.6 g of Si as the absorber material. In this case, an excess power of 6 pW was measured in the phonon sensor arrays, corresponding to an excess substrate power of 18 pW or $10^{-24} \text{ W}\mu\text{m}^{-3}$. As this provides the superior limit, we use the measurement from SuperCDMS-CPD [37]. Note that in Ref. [45], future projections with

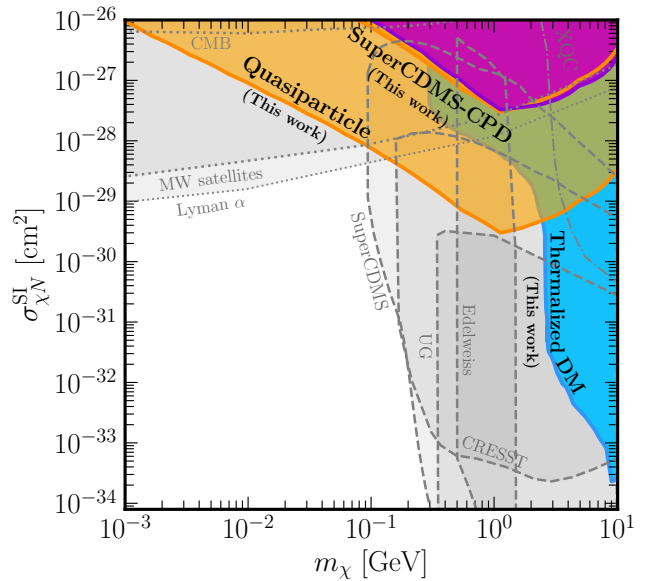


Figure 3. New limits on spin-independent DM-nucleon scattering cross section $\sigma_{\chi N}$ derived in this work, using quantum devices. We show halo DM limits from excess quasiparticle production measurements (orange) and SuperCDMS-CPD (magenta). “Thermalized DM” (blue) is our new constraint on the thermalized DM population, with several experiments overlapping in their exclusion of this population. The gray regions are other existing limits, see text for discussion.

a hypothetically altered version of SuperCDMS were considered for thermalized DM. Here, we already use the current SuperCDMS measurements to set the first limits.

New Dark Matter Constraints.— Figure 3 shows the new bounds we derive for spin-independent DM-SM scattering. The strongest sensitivity is achieved using quasiparticle density measurements. The conversion from quasiparticle density to quasiparticle generation rate can only be trusted to an order of magnitude, and so we show two orange “quasiparticle” lines, representing a conservative and an optimistic constraint, which corresponds to taking $\bar{\Gamma} = 4$ or $400 \text{ s}^{-1}\mu\text{m}^3$ respectively, i.e. moving the quasiparticle generation rate between its expected range of validity. The next strongest bound arises from scattering power injection with SuperCDMS CPD, where we find that their volume advantage still overcomes the superior power sensitivity of the low-noise bolometer, which is too weak to show on the plot for halo DM. The top two bounds correspond to limits using the incoming halo DM, while the blue “thermalized DM” constraint uses only the thermalized DM population.

In Fig. 3, for thermalized DM, all three of our quantum devices approximately overlap in their constraint strength. While the devices all actually have differing sensitivity levels, DM evaporation from the Earth truncates the lower end of our DM mass sensitivity. This occurs due to thermal kicks transferring too much energy to the DM particle relative to the gravitational binding

energy of the Earth, such that DM escapes the Earth and does not remain bound to produce any signal. If it weren't for the DM evaporation rate, our quantum sensors would have sensitivity extending to much lower cross sections for the thermalized DM component. This motivates studies of models that do not evaporate at these DM masses and cross sections. For thermalized DM, largest DM densities are achieved for the asymmetric DM, which we assume for our densities, though we are also sensitive to annihilating DM models; p -wave annihilating DM does also not effect our assumed DM densities [28]. Note that in comparison, the incoming halo DM limits do not require any assumptions about DM annihilation. The halo limits extend to lower masses as incoming DM which later evaporates still leads to a bound from when DM is first entering the Earth. We do not show ceilings for our limits, which will exist but require simulations to calculate accurately. We expect this could lower the limits at large cross sections at the top of Fig. (3). Similarly, the DM evaporation mass threshold at large cross sections for thermalized DM ideally requires simulations, which may weaken our thermalized DM bound, especially for DM below a GeV.

In Fig. 3 we also compare with existing limits, including those from astrophysical systems such as Milky Way satellites [46], Lyman-alpha [47], and the CMB [48]. There are also a number of lab experiments overlapping with part of our parameter space, namely by CRESST [49], SuperCDMS [50], Edelweiss [51], XQC [52], and “UG” which is a combined limit line from deep underground experiments [53–58]. However, there is significant ambiguity in the interpretation at cross sections exceeding about 10^{-30} cm² where the Born approximation breaks down, and the nuclear coherence across different detector materials is not well defined without using a DM model [59, 60]. For transparency we show all bounds that have been quoted in this parameter space, but emphasize many of these bounds are not generic, have different assumptions, and cannot be directly compared in a consistent manner without a DM model [59, 60]. As such, our bounds significantly add to the picture of exclusions on this parameter space, even in the regions where they naively appear to overlap. There are also regions where we only overlap with astrophysical measurements, which are inherently less certain than our lab-based measurements.

Conclusions and Outlook.— We presented existing quantum sensors, which have so far not been used to search for DM, as new DM detectors. We pointed out for the first time that such devices allow a probe of DM through excess quasiparticle generation in single quasiparticle devices, and excess power produced in athermal phonon sensors. We considered DM power deposition in these devices, and their already existing measurements, to constrain two types of DM which potentially exist in the Earth. Firstly, we constrained DM from the incoming Galactic halo above about an MeV. Secondly, we set

limits on the thermalized DM which is already captured and thermalized within the Earth, for MeV-GeV scale DM.

We identified these new DM sensitivities with three different devices. Single quasiparticle devices provide new constraints already, with promise to provide improved results in future, if lower background noise is achieved. The best limit arises from quasiparticle density measurements, in devices aiming for low quasiparticle backgrounds. The quasiparticle density measurement we used from Ref. [35] may also bring new constraints in the future; they noted the device could potentially be adapted to operate as an energy-resolving single-photon detector in the THz range, similar to the low-noise bolometer we discussed.

We also set new constraints using volume-scaled TES bias power measurements, in which the TES is coupled to a large aluminum absorber, as per SuperCDMS detectors. It is likely there is a more stringent constraint on specifically the volumetric power load of cryogenic materials that could rule out further parameter space. For example, a similar constraint could be placed by comparing the heat load on the CUORE cryostat with and without the 2 ton payload, where a $2\mu\text{W}$ difference in power load was observed between the loaded and unloaded states [61], however the systematics on that measurement are not currently sufficiently bounded to be included in our analysis. In future, a larger volume absorber, measured with better systematic controls, would be able to provide stronger constraints on thermal DM.

Intriguingly, we noted that the known quasiparticle “background” already detected in quantum devices could potentially be a positive DM signal. However, given the incomplete treatment of systematics in these measurements, this excess does not at this stage warrant serious attention as a robust DM signal detection, although improved studies of systematics in future will be valuable.

Going forward, our work serves as strong motivation to better understand the systematic uncertainties corresponding to some of these measurements, and motivates further exploration with quantum devices to probe the highly abundant, low velocity, thermalized DM population. Moreover, the encouraging results obtained here will inspire future study to optimize the absorber material for low velocity DM detection. Furthermore, the constraints we already obtained on incoming halo DM are stronger than any existing direct detection experiment, with promise for future improvement.

Acknowledgments.— We thank Tongyan Lin, Robert McDermott, Britton Plourde, Matt Pyle, and Juri Smirnov for helpful discussions and comments. AD and RKL are supported by the U.S. Department of Energy under Contract DE-AC02-76SF00515. NK is supported by the US. Department of Energy Early Career Research Program (ECRP) under FWP 100872.

Dark Matter Induced Power in Quantum Devices

Supplemental Material

Anirban Das, Noah Kurinsky, and Rebecca K. Leane

CONTENTS

I.	Details of Phonon Production	1
	A. Formalism	1
	B. The Phonon Density of State and Structure Factor	2
	C. Number of Phonons Excited	3
II.	Regimes of Validity: Phonon Excitation or Nuclear Recoil?	3
	References	4

I. DETAILS OF PHONON PRODUCTION

A. Formalism

When the DM energy is low enough that the typical momentum transfer is comparable to the average inverse width of nuclear wavefunction ($q_{\text{nuc}} \sim \sqrt{2m_A\bar{\omega}}$) in the detector material, collective excitation of the atoms becomes important in the calculation of the response of the detector. For thermalized DM near the surface of the Earth, the typical energy is $E_{\text{DM}} \simeq 26$ meV and momentum $q \gtrsim 10$ keV which is well within the regime where lattice vibrations or phonon excitations due to DM scattering become important (similarly for light DM from the halo). As we will now show, both the energy and momentum play significant role in determining the scattering rate.

The momentum transfer q dictates how the atoms from different lattice sites respond collectively. Following Ref. [32, 33], we use the value of q to separate the scattering into two regimes. When $q < q_{\text{BZ}} (= 2\pi/a)$, the phonon wavelength is greater than the lattice size a . In this case, the excitation extends over multiple atoms and the scattering is *coherent*. However, for $q > q_{\text{BZ}}$ the phonons have short wavelength and responses from different lattice sites do not interfere. This is the *incoherent* scattering regime.

In the most general case, the structure factor $S(\mathbf{q}, \omega)$ can be written as a sum over the responses from all lattice sites and atoms of a homogeneous crystal,

$$S(\mathbf{q}, \omega) = \sum_{l, l'}^N \sum_{d, d'}^m \overline{f_{d'}^* f_d} C_{l'd'ld}. \quad (\text{S1})$$

Here, l is the lattice index, d is the inequivalent atom index within a primitive cell, N is the number of primitive cells in a volume V , m is the number of inequivalent atoms in a primitive cell, and $C_{l'd'ld}$ is the time-dependent two-point correlation function for lattice points l and l' , atoms d and d' within them,

$$C_{l'd'ld} \equiv \frac{1}{V} \int_{-\infty}^{+\infty} dt \langle e^{-i\mathbf{q} \cdot \mathbf{u}_{l'd'}(0)} e^{i\mathbf{q} \cdot \mathbf{u}_{ld}(t)} \rangle e^{-i\omega t}, \quad (\text{S2})$$

with \mathbf{u}_{ld} as the displacement vector of the d -th atom in l -th lattice cell. For incoherent regime, we are not interested in the interferences in the sum in Eq. (S1). Hence,

$$S(\mathbf{q}, \omega) \approx \sum_l^N \sum_d^m \left(\overline{f_d^2} - (\overline{f_d})^2 \right) C_{ld}. \quad (\text{S3})$$

Upon further simplification, Eq. (S2) takes the form,

$$C_{l'd'ld} \equiv \frac{1}{V} \int_{-\infty}^{+\infty} dt e^{-2W_d(\mathbf{q})} e^{i\mathbf{q} \cdot \mathbf{u}_{l'd'}(0) - i\mathbf{q} \cdot \mathbf{u}_{ld}(t)} e^{-i\omega t}. \quad (\text{S4})$$

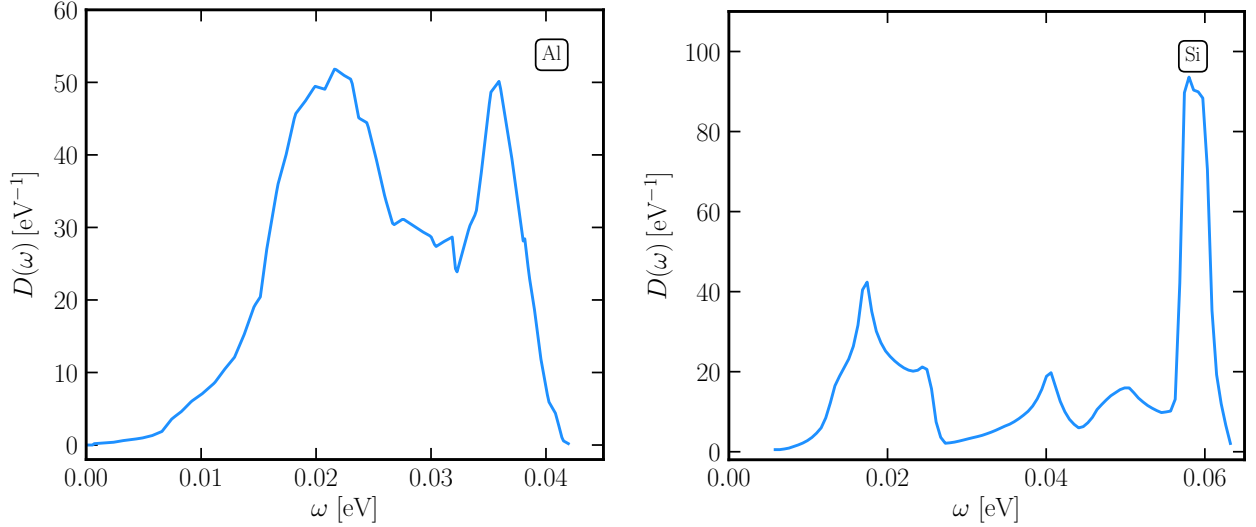


Figure S1. The phonon density of state as a function of energy, for aluminum (*left*) and silicon (*right*). For Al, the features are due to the transverse and longitudinal acoustic phonon branches. In Si, the rightmost peak is due the optical phonon branch.

After quantizing the lattice displacement vector \mathbf{u}_{ld} , the quantity $\langle \mathbf{q} \cdot \mathbf{u}_{ld'}(0) \mathbf{q} \cdot \mathbf{u}_{ld'}(t) \rangle$ can be simplified to

$$\langle \mathbf{q} \cdot \mathbf{u}_{ld'}(0) \mathbf{q} \cdot \mathbf{u}_{ld'}(t) \rangle \approx \frac{q^2}{3} \sum_{\nu} \sum_{\mathbf{k}} \frac{|\mathbf{e}_{\nu, \mathbf{k}, d}|^2}{2Nm_d \omega_{\nu, \mathbf{k}}} e^{i\omega_{\nu, \mathbf{k}} t} \quad (\text{S5})$$

$$= \frac{q^2}{2m_d} \int_{-\infty}^{+\infty} d\omega \frac{D_d(\omega)}{\omega} e^{i\omega t}. \quad (\text{S6})$$

Here, $D_d(\omega)$ is the partial phonon DoS of d -th atom. This expression can be used to write a general form of C_{ld} for n number of phonon excitation with isotropic assumption,

$$C_{ld} = \frac{2\pi}{V} e^{-2W_d(\mathbf{q})} \sum_n \frac{1}{n!} \left(\frac{q^2}{2m_d} \right)^n \left(\prod_{i=1}^n \int d\omega_i \frac{D_d(\omega_i)}{\omega_i} \right) \delta \left(\omega - \sum_i \omega_i \right). \quad (\text{S7})$$

with the Debye-Waller function given by

$$W_d(\mathbf{q}) = \frac{q^2}{4m_d} \int d\omega \frac{D_d(\omega)}{\omega}. \quad (\text{S8})$$

Finally, using Eq. (S7) in Eq. (S3) yields the structure factor in Eq. (6).

B. The Phonon Density of State and Structure Factor

Figure S1 shows the phonon DoS $D(\omega)$ for both aluminium (left) and silicon (right), which are the detector materials we have focused on. Al has a face-centered-cubic crystal structure with only one atom in the primitive cell. Hence, it has only an acoustic phonon branch, which is the phonon branch when all atoms oscillate in phase. The two clear peaks in the Al DoS are due to the transverse and longitudinal acoustic branches. Si, on the other hand, has diamond crystal structure with two inequivalent atoms in its primitive cell. Hence, in addition to acoustic branches, it has optical phonon branches, which arise when neighboring atoms oscillate in opposite phase. Compared to acoustic phonon branches, the optical branch adds more phonon states at higher energies [62], although low-velocity thermalized DM does not exploit this feature. The rightmost peak at $\omega \simeq 0.06$ eV is due to the optical branches. The phonon DoS is important for understanding which energies can have resonant energy transfers and result in large scattering rates. For example, the features in the differential scattering rates in Fig. 2 can be associated with the corresponding features in the DoS shown above. The $\sim 1/\bar{\omega}_d$ dependence of $S(q, \omega)$ in Eq. (6) suppresses the rate at higher energy.

Figure S2 shows the incoherence structure factor for aluminium (left) and silicon (right), as well as the DM phase space for thermalized DM with $m_\chi = 1$ and 10 GeV. Below q_{BZ} , only narrow regions along the ω_{LA} and ω_{LO} lines can

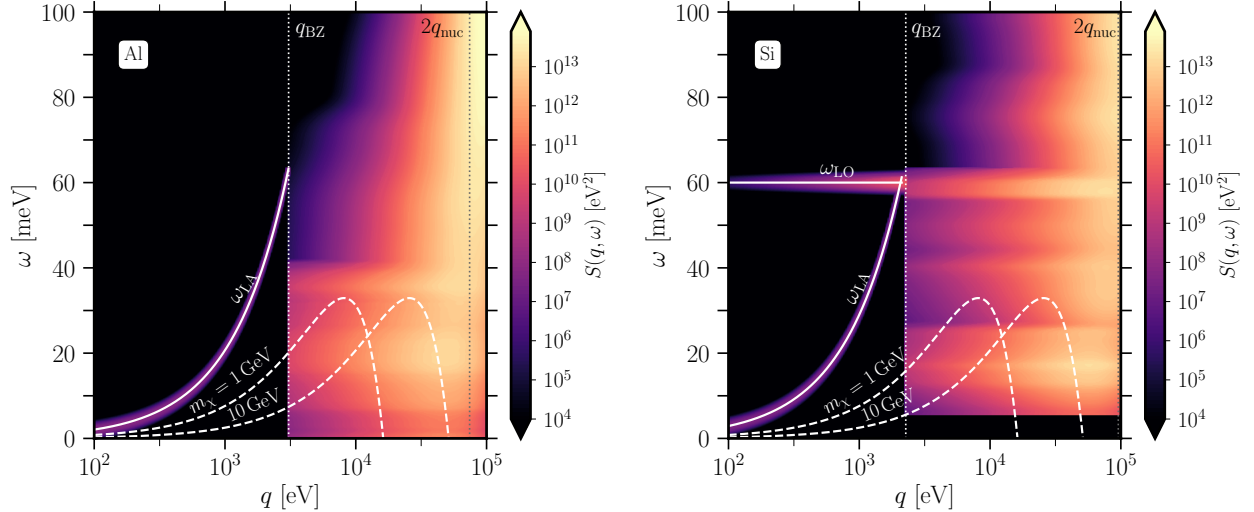


Figure S2. The incoherent structure factor $S(q, \omega)$ as a function of momentum q and phonon energy ω for aluminum (left) and silicon (right). Below the inverse lattice constant q_{BZ} the scattering is incoherent. The longitudinal acoustic and optical branches, labeled as ω_{LA} and ω_{LO} respectively, are shown in solid white lines. We broadened the structure factor along these lines with a 0.5 meV due to finite phonon decay width. Above q_{BZ} in the incoherent regime, the bright bands are due to the varying number of phonon excitations. Above the inverse length of the nuclear wavefunction q_{nuc} , the scattering can be approximated through nuclear recoils rather than phonon excitations. The thermalized DM phase spaces for $m_\chi = 1$ and 10 GeV are marked with dashed white lines.

be excited. We choose a finite width of 0.5 meV along the lines which approximates realistic phonon decay lifetimes. At low momentum, the acoustic branch has a dispersion $\omega \sim q$, whereas the optical branch dispersion is assumed to be constant in q for simplicity. Above q_{BZ} , the structure factor broadens due to multiple phonon excitations.

In Fig. S2, the DM phase spaces are marked with white dashed lines (see Eq. (3) for the definition). These shapes vary greatly from galactic halo DM phase spaces, as thermalized DM does not increase its maximum energy with mass as it is thermalized with temperature $T_\chi \simeq 300 \text{ K}$. To compare coherent and incoherent scattering regimes, we note that the lattice constants of Al and Si are 4.05 \AA and 5.43 \AA , respectively. They correspond to Brillouin zone boundaries $q_{\text{BZ}} = 3.06 \text{ keV}$ and 2.3 keV in the Fourier space. Therefore, even though thermalized DM has lower kinetic energy than the galactic halo DM, these momenta fall below the typical momenta of such DM of mass between 1 and 10 GeV . Moreover, a large part of them lie above q_{BZ} in both cases. Therefore, the incoherent scattering dominates the scattering rate.

C. Number of Phonons Excited

It is also interesting to ask the average number of phonon excited per single DM scattering. This can be estimated by $n \sim q^2 / (2m_A \bar{\omega})$. We find $\bar{\omega} = 25.5$ and 40.8 meV for Al and Si, respectively. For $m_\chi = 1 \text{ GeV}$ with a maximum momentum transfer of $q = 20 \text{ keV}$, this yields $n = 0.29$ and 0.18 , respectively. For comparison, halo DM of the same mass can have maximum momentum $q = 0.73 \text{ MeV}$ corresponding to $n \gg 1$. This is because thermalized DM has less kinetic energy than its halo counterpart. Finally, we note that because of the lower energy, the overlap between the DM phase space and $S(q, \omega)$ is not optimal for either of Al and Si. A material with more states at low energy $\omega \lesssim 30 \text{ meV}$ could yield higher energy transfer to the detector from thermalized DM. We leave further investigation in this direction to future work.

II. REGIMES OF VALIDITY: PHONON EXCITATION OR NUCLEAR RECOIL?

Finally, we would like to emphasize that the relevant degrees of freedom in a detector material depends on the typical momentum and energy of the scattering DM particles. The critical momentum scale in this case is the average inverse width of nuclear wavefunction $q_{\text{nuc}} \sim \sqrt{2m_A \bar{\omega}}$ [29, 30, 32]. Note that $q_{\text{nuc}} = 37.1$ and 47.8 keV for Al and Si respectively. If the typical DM momentum $q_{\text{DM}} \lesssim q_{\text{nuc}}$, then the energy deposition occurs mainly by phonon

excitation, and the atoms are not free particles. On the other hand, only when $q_{\text{DM}} > 2q_{\text{nuc}}$, single nuclear recoil becomes an appropriate description of the scattering process. Thermalized DM with $T_{\chi} \simeq 300$ K can have a maximum momentum transfer

$$q_{\text{max}} = 6.37 \text{ keV} \left(\frac{m_{\chi}}{1 \text{ GeV}} \right)^{\frac{1}{2}}. \quad (\text{S9})$$

Clearly, this is smaller than q_{nuc} for all DM masses below $m_{\chi} \lesssim 35$ GeV. Therefore, phonon excitation is the appropriate treatment for our parameter space.

-
- [1] J. Aalbers *et al.* (LUX-ZEPLIN), (2022), [arXiv:2207.03764 \[hep-ex\]](#).
- [2] J. D. Vergados and H. Ejiri, *Phys. Lett. B* **606**, 313 (2005), [arXiv:hep-ph/0401151](#).
- [3] C. C. Moustakidis, J. D. Vergados, and H. Ejiri, *Nucl. Phys. B* **727**, 406 (2005), [arXiv:hep-ph/0507123](#).
- [4] R. Bernabei *et al.*, *Int. J. Mod. Phys. A* **22**, 3155 (2007), [arXiv:0706.1421 \[astro-ph\]](#).
- [5] M. Ibe, W. Nakano, Y. Shoji, and K. Suzuki, *JHEP* **03**, 194 (2018), [arXiv:1707.07258 \[hep-ph\]](#).
- [6] E. Aprile *et al.* (XENON), *Phys. Rev. Lett.* **123**, 241803 (2019), [arXiv:1907.12771 \[hep-ex\]](#).
- [7] J. Tiffenberg, M. Sofo-Haro, A. Drlica-Wagner, R. Essig, Y. Guardincerri, S. Holland, T. Volansky, and T.-T. Yu (SENSEI), *Phys. Rev. Lett.* **119**, 131802 (2017), [arXiv:1706.00028 \[physics.ins-det\]](#).
- [8] L. Barak *et al.* (SENSEI), *Phys. Rev. Lett.* **125**, 171802 (2020), [arXiv:2004.11378 \[astro-ph.CO\]](#).
- [9] E. Aprile *et al.* (XENON), *Phys. Rev. Lett.* **123**, 251801 (2019), [arXiv:1907.11485 \[hep-ex\]](#).
- [10] Y. Hochberg, Y. F. Kahn, R. K. Leane, S. Rajendran, K. Van Tilburg, T.-T. Yu, and K. M. Zurek, *Nature Rev. Phys.* **4**, 637 (2022).
- [11] Y. Hochberg, Y. Zhao, and K. M. Zurek, *Phys. Rev. Lett.* **116**, 011301 (2016), [arXiv:1504.07237 \[hep-ph\]](#).
- [12] Y. Hochberg, M. Pyle, Y. Zhao, and K. M. Zurek, *JHEP* **08**, 057 (2016), [arXiv:1512.04533 \[hep-ph\]](#).
- [13] Y. Hochberg, Y. Kahn, N. Kurinsky, B. V. Lehmann, T. C. Yu, and K. K. Berggren, *Phys. Rev. Lett.* **127**, 151802 (2021), [arXiv:2101.08263 \[hep-ph\]](#).
- [14] Y. Hochberg, E. D. Kramer, N. Kurinsky, and B. V. Lehmann, (2021), [arXiv:2109.04473 \[hep-ph\]](#).
- [15] Y. Hochberg, I. Charaev, S.-W. Nam, V. Verma, M. Colangelo, and K. K. Berggren, *Phys. Rev. Lett.* **123**, 151802 (2019), [arXiv:1903.05101 \[hep-ph\]](#).
- [16] J. Chiles *et al.*, *Phys. Rev. Lett.* **128**, 231802 (2022), [arXiv:2110.01582 \[hep-ex\]](#).
- [17] K. Schutz and K. M. Zurek, *Phys. Rev. Lett.* **117**, 121302 (2016), [arXiv:1604.08206 \[hep-ph\]](#).
- [18] S. Knapen, T. Lin, and K. M. Zurek, *Phys. Rev. D* **95**, 056019 (2017), [arXiv:1611.06228 \[hep-ph\]](#).
- [19] A. Caputo, A. Esposito, and A. D. Polosa, *Phys. Rev. D* **100**, 116007 (2019), [arXiv:1907.10635 \[hep-ph\]](#).
- [20] S. Griffin, S. Knapen, T. Lin, and K. M. Zurek, *Phys. Rev. D* **98**, 115034 (2018), [arXiv:1807.10291 \[hep-ph\]](#).
- [21] S. Knapen, T. Lin, M. Pyle, and K. M. Zurek, *Phys. Lett. B* **785**, 386 (2018), [arXiv:1712.06598 \[hep-ph\]](#).
- [22] P. Cox, T. Melia, and S. Rajendran, *Phys. Rev. D* **100**, 055011 (2019), [arXiv:1905.05575 \[hep-ph\]](#).
- [23] M.-A. Sánchez-Martínez, I. n. Robredo, A. Bidauzarraga, A. Bergara, F. de Juan, A. G. Grushin, and M. G. Vergniory, *Materials* **3**, 014001 (2019), [arXiv:1905.04805 \[cond-mat.mtrl-sci\]](#).
- [24] Y. Hochberg, Y. Kahn, M. Lisanti, K. M. Zurek, A. G. Grushin, R. Ilan, S. M. Griffin, Z.-F. Liu, S. F. Weber, and J. B. Neaton, *Phys. Rev. D* **97**, 015004 (2018), [arXiv:1708.08929 \[hep-ph\]](#).
- [25] R. M. Geilhufe, B. Olsthoorn, A. Ferella, T. Koski, F. Kahlhoefer, J. Conrad, and A. V. Balatsky, *Phys. Status Solidi RRL* **12**, 1800293 (2018), [arXiv:1806.06040 \[cond-mat.mtrl-sci\]](#).
- [26] R. M. Geilhufe, F. Kahlhoefer, and M. W. Winkler, *Phys. Rev. D* **101**, 055005 (2020), [arXiv:1910.02091 \[hep-ph\]](#).
- [27] A. Coskuner, A. Mitridate, A. Olivares, and K. M. Zurek, *Phys. Rev. D* **103**, 016006 (2021), [arXiv:1909.09170 \[hep-ph\]](#).
- [28] R. K. Leane and J. Smirnov, (2022), [arXiv:2209.09834 \[hep-ph\]](#).
- [29] Y. Kahn and T. Lin, *Rept. Prog. Phys.* **85**, 066901 (2022), [arXiv:2108.03239 \[hep-ph\]](#).
- [30] T. Trickle, Z. Zhang, K. M. Zurek, K. Inzani, and S. M. Griffin, *JHEP* **03**, 036 (2020), [arXiv:1910.08092 \[hep-ph\]](#).
- [31] S. Knapen, J. Kozaczuk, and T. Lin, *Phys. Rev. D* **105**, 015014 (2022), [arXiv:2104.12786 \[hep-ph\]](#).
- [32] B. Campbell-Deem, S. Knapen, T. Lin, and E. Villarama, (2022), [arXiv:2205.02250 \[hep-ph\]](#).
- [33] G. L. Squires, *Introduction to the theory of thermal neutron scattering*.
- [34] B. Campbell-Deem, P. Cox, S. Knapen, T. Lin, and T. Melia, *Phys. Rev. D* **101**, 036006 (2020), [Erratum: *Phys. Rev. D* **102**, 019904 (2020)], [arXiv:1911.03482 \[hep-ph\]](#).
- [35] E. T. Mannila, P. Samuëlsson, S. Simbierowicz, J. T. Peltonen, V. Vesterinen, L. Grönberg, J. Hassel, V. F. Maisi, and J. P. Pekola, *Nature Physics* **18**, 145 (2021).
- [36] P. M. Echternach, B. J. Pepper, T. Reck, and C. M. Bradford, *Nature Astronomy* **2**, 90 (2018).
- [37] C. W. Fink, S. L. Watkins, T. Aramaki, P. L. Brink, J. Camilleri, X. Defay, S. Ganjam, Y. G. Kolomensky, R. Mahapatra, N. Mirabolfathi, W. A. Page, R. Partridge, M. Platt, M. Pyle, B. Sadoulet, B. Serfass, and S. Z. and, *Applied Physics Letters* **118**, 022601 (2021).
- [38] R. Ren, C. Bathurst, Y. Chang, R. Chen, C. Fink, Z. Hong, N. Kurinsky, N. Mast, N. Mishra, V. Novati, G. Spahn, H. M. zu Theenhausen, S. Watkins, Z. Williams, M. Wilson, A. Zaytsev, D. Bauer, R. Bunker, E. Figueroa-Feliciano,

- M. Hollister, L. Hsu, P. Lukens, R. Mahapatra, N. Mirabolfathi, B. Nebolsky, M. Platt, F. Ponce, M. Pyle, T. Reynolds, and T. Saab, *Physical Review D* **104** (2021), [10.1103/physrevd.104.032010](https://doi.org/10.1103/physrevd.104.032010).
- [39] S. B. Kaplan, C. C. Chi, D. N. Langenberg, J. J. Chang, S. Jafarey, and D. J. Scalapino, *Phys. Rev. B* **14**, 4854 (1976).
- [40] A. Bepalov, M. Houzet, J. S. Meyer, and Y. V. Nazarov, *Physical Review Letters* **117** (2016), [10.1103/physrevlett.117.117002](https://doi.org/10.1103/physrevlett.117.117002).
- [41] A. Vepsalainen *et al.*, *Nature* **584**, 551 (2020), [arXiv:2001.09190](https://arxiv.org/abs/2001.09190) [quant-ph].
- [42] L. Cardani *et al.*, *Nature Commun.* **12**, 2733 (2021), [arXiv:2005.02286](https://arxiv.org/abs/2005.02286) [cond-mat.supr-con].
- [43] C. D. Wilen *et al.*, *Nature* **594**, 369 (2021), [arXiv:2012.06029](https://arxiv.org/abs/2012.06029) [quant-ph].
- [44] J. M. Martinis, “Saving superconducting quantum processors from qubit decay and correlated errors generated by gamma and cosmic rays,” (2020).
- [45] J. Billard, M. Pyle, S. Rajendran, and H. Ramani, (2022), [arXiv:2208.05485](https://arxiv.org/abs/2208.05485) [hep-ph].
- [46] E. O. Nadler *et al.* (DES), *Phys. Rev. Lett.* **126**, 091101 (2021), [arXiv:2008.00022](https://arxiv.org/abs/2008.00022) [astro-ph.CO].
- [47] K. K. Rogers, C. Dvorkin, and H. V. Peiris, *Phys. Rev. Lett.* **128**, 171301 (2022), [arXiv:2111.10386](https://arxiv.org/abs/2111.10386) [astro-ph.CO].
- [48] W. L. Xu, C. Dvorkin, and A. Chael, *Phys. Rev. D* **97**, 103530 (2018), [arXiv:1802.06788](https://arxiv.org/abs/1802.06788) [astro-ph.CO].
- [49] G. Angloher *et al.* (CRESST), *Eur. Phys. J. C* **77**, 637 (2017), [arXiv:1707.06749](https://arxiv.org/abs/1707.06749) [astro-ph.CO].
- [50] I. Alkhatib *et al.* (SuperCDMS), *Phys. Rev. Lett.* **127**, 061801 (2021), [arXiv:2007.14289](https://arxiv.org/abs/2007.14289) [hep-ex].
- [51] E. Armengaud *et al.* (EDELWEISS), *Phys. Rev. D* **99**, 082003 (2019), [arXiv:1901.03588](https://arxiv.org/abs/1901.03588) [astro-ph.GA].
- [52] M. S. Mahdawi and G. R. Farrar, *JCAP* **10**, 007 (2018), [arXiv:1804.03073](https://arxiv.org/abs/1804.03073) [hep-ph].
- [53] F. Petricca *et al.* (CRESST), *J. Phys. Conf. Ser.* **1342**, 012076 (2020), [arXiv:1711.07692](https://arxiv.org/abs/1711.07692) [astro-ph.CO].
- [54] R. Agnese *et al.* (SuperCDMS), *Phys. Rev. D* **97**, 022002 (2018), [arXiv:1707.01632](https://arxiv.org/abs/1707.01632) [astro-ph.CO].
- [55] D. S. Akerib *et al.* (LUX), *Phys. Rev. Lett.* **118**, 021303 (2017), [arXiv:1608.07648](https://arxiv.org/abs/1608.07648) [astro-ph.CO].
- [56] E. Aprile *et al.* (XENON), *Phys. Rev. Lett.* **119**, 181301 (2017), [arXiv:1705.06655](https://arxiv.org/abs/1705.06655) [astro-ph.CO].
- [57] X. Cui *et al.* (PandaX-II), *Phys. Rev. Lett.* **119**, 181302 (2017), [arXiv:1708.06917](https://arxiv.org/abs/1708.06917) [astro-ph.CO].
- [58] D. Hooper and S. D. McDermott, *Phys. Rev. D* **97**, 115006 (2018), [arXiv:1802.03025](https://arxiv.org/abs/1802.03025) [hep-ph].
- [59] M. C. Digman, C. V. Cappiello, J. F. Beacom, C. M. Hirata, and A. H. G. Peter, *Phys. Rev. D* **100**, 063013 (2019), [arXiv:1907.10618](https://arxiv.org/abs/1907.10618) [hep-ph].
- [60] X. Xu and G. R. Farrar, (2020), [arXiv:2101.00142](https://arxiv.org/abs/2101.00142) [hep-ph].
- [61] C. Alduino, F. Alessandria, M. Balata, D. Biare, M. Biassoni, C. Bucci, A. Caminata, L. Canonica, L. Cappelli, G. Ceruti, A. Chiarini, N. Chott, M. Clemenza, S. Copello, A. Corsi, O. Cremonesi, A. D’Addabbo, S. Dell’Oro, L. D. Paolo, M. D. Vacri, A. Drobizhev, M. Faverezani, E. Ferri, M. Franceschi, R. Gaigher, L. Gladstone, P. Gorla, M. Guetti, L. Ioannucci, Y. Kolomensky, C. Ligi, L. Marini, T. Napolitano, S. Nisi, A. Nucciotti, I. Nutini, T. O’Donnell, D. Orlandi, J. Ouellet, C. Pagliarone, L. Pattavina, A. Pelosi, M. Peregò, E. Previtalli, B. Romualdi, A. Rotilio, C. Rusconi, D. Santone, V. Singh, M. Sisti, L. Taffarello, E. Tatananni, F. Terranova, S. Wagaarachchi, J. Wallig, and C. Zarra, *Cryogenics* **102**, 9 (2019).
- [62] C. Kittel, *Introduction to Solid State Physics*, 8th ed. (Wiley, 2004).